Effects of Defect and Temperature on the Mechanical Performance of WS_2 A Multiscale Analysis

Tang, Hongyu; Hu, Dong; Cui, Zhen; Ye, Huaiyu; Zhang, Guoqi

DOI
10.1021/acs.jpcc.0c09897

Publication date
2021

Document Version
Final published version

Published in
Journal of Physical Chemistry C

THE JOURNAL OF PHYSICAL CHEMISTRY C
A JOURNAL OF THE AMERICAN CHEMICAL SOCIETY

pubs.acs.org/JPCC

Article

Effects of Defect and Temperature on the Mechanical Performance of WS_2: A Multiscale Analysis

Hongyu Tang,[‖] Dong Hu,[‖] Zhen Cui, Huaiyu Ye, and Guoqi Zhang*

Cite This: J. Phys. Chem. C 2021, 125, 2680–2690

Read Online

ACCESS | Metrics & More | Article Recommendations | Supporting Information

ABSTRACT: This paper analyzes the mechanical properties of tungsten disulfide (WS_2) by means of multiscale simulation, including density functional theory (DFT), molecular dynamic (MD) analysis, and finite element analysis (FEA). We first conducted MD analysis to calculate the mechanical properties (i.e., Young's modulus and critical stress) of WS_2. The influence of different defect types (i.e., point defects and line defects) on the mechanical properties are discussed. The results reveal that WS_2 has a high Young's modulus and high critical stress. Next, the effects of defect density and temperature on the mechanical properties of the material were analyzed. The results show that a lower defect density results in improved performance and a higher temperature results in better ductility, which indicate that WS_2 can potentially be a strain sensor. Based on this result, FEA was employed to analyze the WS_2 stress sensor and then fabricate and analyze the device for benchmarking. It is found that the FEA model proposed in this work can be used for further optimization of the device. According to the DFT results, a narrower band gap WS_2 is found with the existence of defects and the applied strain. The proposed multiscale simulation method can effectively analyze the mechanical properties of WS_2 and optimize the design. Moreover, this method can be extended to other 2D/nanomaterials, providing a reference for a rapid and effective systematic design from the nanoscale to macroscale.

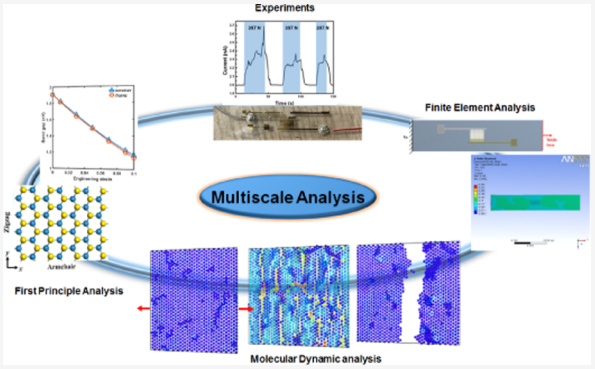

1. INTRODUCTION

After graphene was discovered in 2004, various two-dimensional (2D) materials beyond graphene, such as transition-metal dichalcogenides (TMDCs), MXenes, and metal oxides, have attracted extensive attention worldwide.[1] Tungsten sulfide (WS_2), as a semiconductor of TMDCs, consists of three atomic layers of W layers sandwiched between two S layers, which enable its Young's modulus to be 236 ± 65 GPa that is comparable to that of steel.[2] It has an indirect band gap of ~1.9 eV and unique chemical properties, which indicate that WS_2 has great potential to be applied in photonics, gas sensors, and transistors.[3−7] Benefit from high Young's modulus, WS_2 has been widely used for flexible devices, such as E-skin and wearable sensors.[8] Recently, the 2D elastic moduli and Poisson's ratios derived from first-principles density functional theory (DFT) calculations are 137 N/m and 0.22 for WS_2, respectively.[9] Zhang et al.[10] investigated the strain relaxation of monolayer WS_2 triangular crystals deposited on a polydimethylsiloxane substrate. They found that the optical spectra of monolayer WS_2 depended on the range and direction of tensile strain. Guo et al.[11] used WS_2 in a humidity sensor for flexible electronic skin. Qi et al.[12] deposited WS_2 onto a polyethylene terephthalate (PET) substrate and obtained a high-sensitive, flexible, and transparent sensor with a gauge factor (GF) of 14. However, few people considered the influence of defects on the electrical, optical, and mechanical properties of WS_2.

Different from the simple monovacancy in graphene, WS_2 has more complicated defects because of its sandwiched structure.[13] It is known that the WS_2 monolayer exhibits naturally formed vacancies, such as S vacancy (V_S) and W vacancy (V_W), which have significant impacts on the electrical and optical properties. Through DFT analysis, Zhao et al.[14] demonstrated that intrinsic three tungsten vacancies (V_{3W}), six sulfur vacancies (V_{6S}), and 1W + 2S vacancies (V_{1W+2S}) could induce a total spin magnetic moment. Schuler et al.[15] analyzed the effects of four different substitutional defects on the charge localization and optical properties of WS_2 through experimental and theoretical analyses. Except for pristine defects, the defects induced by external tensile strain will significantly affect the performance of WS_2. Wang et al.[16] predicted the influence of crack edge chirality and tip configuration on the fracture

Received: November 2, 2020
Revised: January 8, 2021
Published: January 20, 2021

toughness and crack propagation path of monolayer MoS_2. However, few researchers focus on the defects' influence on the mechanical properties of WS_2, which hinders its applications in strain sensors.

Multiscale simulations for 2D materials have been studied in different length scales, including atomic, molecular, and device-level modeling.[17,18] Mashhadzadeh et al.[19−22] analyzed the mechanical properties of various nanomaterials based on molecular dynamics (MD) simulations. They also used a multiscale finite element model to study the tensile modulus of graphene-reinforced polypropylene nanocomposites and compare the results with experimental tensile tests. Kumar et al.[23] demonstrated that interlayer interactions of three different bilayer structures can cause band gap change by using a multiscale computational method. The elastic deformations for general bilayer structures have been established and validated via comparing the deformations with MD simulations as well as with experiments for graphene/hBN bilayer heterostructures. The electrical, optical, and gas sensing properties of 2D materials have been analyzed through first-principles analysis.[24,25] However, it is a lack of multiscale approach to systematically analyze the mechanical properties of WS_2 with defects.

In this study, we first perform systematic MD simulations to investigate the mechanical properties of WS_2 without and with defects under tensile strain in armchair (AC) and zigzag (ZZ) directions. The defected WS_2 involves the fracture of WS_2 with initial AC and ZZ cracks and 5−8−5 defects. The mechanical behaviors of WS_2 are studied across different defect densities and different temperatures. Moreover, we predict the potential applications of WS_2 in the strain sensor through finite element analysis (FEA) and experiments. Finally, first-principles analysis is employed to study the influence of engineering strain on the band structure of WS_2.

2. MULTISCALE COMPUTATIONAL METHODS

2.1. First-Principles Analysis Method. All first-principles calculations were carried out within the DFT method by Materials Studio software.[26] The generalized gradient approximation with the Perdew−Burke−Ernzerhof functional was employed. A double-sized numerical basis set plus polarized p-functional was used for our calculations. To describe the van der Waals interactions, the DFT-*D* (*D* stands for dispersion) method with TS correction was adopted.[27] The kinetic energy cutoff of the plane wave was set to 500 eV on a Monkhorst−Pack special *k*-point scheme of 7 × 7 × 1 for geometry optimization and 12 × 12 × 1 *k*-points for band structure calculations. The maximum force and maximum displacement were set to be 0.002 Ha $Å^{-1}$ and 1.0 × 10^{-5} Å, respectively. The convergence criterion for the force between atoms was 0.03 eV $Å^{-1}$. Periodic boundary conditions were applied in the *x* and *y* directions. A 2 × 2 × 1 supercell with an adequate 20 Å vacuum region was introduced to prevent the interactions between the adjacent layers (Figure 1).

2.2. MD Model and Methods. To investigate the deformation and fracture properties of WS_2, MD simulations were carried out using the Large-scale Atomic/Molecular Massively Parallel Simulator (LAMMPS) package.[28] Periodic boundary conditions are applied in all three dimensions. A monolayer WS_2 model was placed at the center of the simulation box as a square domain with side lengths of 75−150 Å, containing 1773 to 7452 atoms. The AC and ZZ edges are oriented along the *x* and *y* directions, respectively. Besides, a

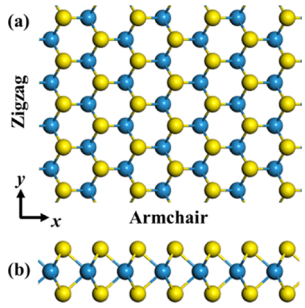

Figure 1. Schematic of the (a) top view and side view of defect-free WS_2. W atoms are shown in blue, whereas S atoms are shown in yellow.

60 Å vacuum space is added upon the monolayer of WS_2. The monolayer WS_2 consist of pairwise (W−S, W−W, and S−S) and angle-bending (S−W−S and W−S−W) interatomic interactions. Atomic interactions through WS_2 were described by the Stillinger−Weber (SW) potential.[29,30] Zhang et al.[31] did a theoretical prediction of superhigh-performance thermoelectric materials based on MoS_2/WS_2 hybrid nanoribbons combined with first-principles calculations and MD simulations. They verified the feasibility of SW potential in MD through DFT calculations. The fitted SW parameters for monolayer WS_2 are listed in Tables S1 and S2. The velocities of atoms were randomly assigned with the Gaussian distribution at the target tension temperature. Newton's equation of motion was integrated with the Verlet algorithm. To stabilize the structure, the energy of the system was minimized by using the conjugate gradient algorithm. Therefore, after energy minimization, the models were first relaxed at a target temperature (200−600 K) in the isothermal−isobaric ensemble with a Nose−Hoover thermostat for 50 ps, to reach their equilibrium state. The external pressure on the simulation box was removed to avoid the influence caused by the pressure variation. Then, the tension simulation at the target temperature was also implemented in the isothermal−isobaric ensemble. Deformation was achieved by changing the shape of the simulation box in the tension direction with a constant strain rate of 0.001 ps^{-1}. The tension simulation stops until the engineering strain reaches 0.3. The velocity Verlet scheme with a time step of 1 fs was utilized for time integration. The average stress for the entire system was calculated by using the formula introduced by Surblys et al.[32] to get the stress−strain curves of the tension simulation

$$\sigma_{ab} = -\frac{1}{V}\left[\frac{1}{2}\sum_{i}\sum_{n=1}^{N_p}\left(r_{1_a}F_{1_b} + r_{2_a}F_{2_b}\right) + \sum_{i} m v_a v_b\right] \quad (1)$$

where *a* and *b* take on values *x*, *y*, *z* to generate the different stress vectors. The first term represents the viral contribution caused by intra- and intermolecular interactions. N_p is the neighbor of atom *i*; r_1 and r_2 represent the positions of the atoms in the pairwise interaction; and F_1 and F_2 are the forces on the atoms resulting from the pairwise interaction. The second term is the kinetic energy contribution to the total stress, where *m* is the mass and *v* is the velocity. Besides, *V* is the total volume of the system. In terms of uniaxial tension simulation, only the component vector on the loading direction was extracted as the stress at a specific strain. The atomic configurations were visualized by Open Visualization Tool (OVITO).[33]

https://dx.doi.org/10.1021/acs.jpcc.0c09897
J. Phys. Chem. C 2021, 125, 2680−2690

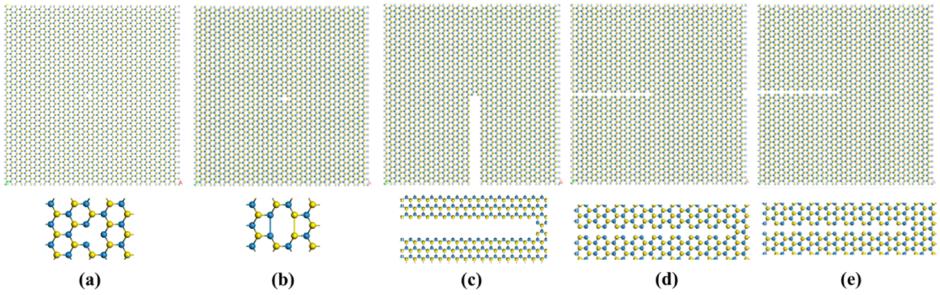

Figure 2. Schematic of the (a) top view and side view of six crack types in WS_2: point defects of (a) 2S vacancies and (b) 5−8−5 defect; line defects of (c) ZZ crack, (d) AC-S crack, and (e) AC-W crack. W atoms are shown in blue, whereas S atoms are shown in yellow.

Figure 3. Schematic of the WS_2-based flexible device.

For studying the effects of natural defects in WS_2, two kinds of point defect, an S vacancy and a 5−8−5 defect, are presented in the center of WS_2, as shown in Figure 2a,b. The 5−8−5 defect is a kind of point defect associated with a "pentagon−octagon−pentagon" configuration of W and S atoms. For studying the crack edge chirality and the crack tip structure, two kinds of line cracks, ZZ cracks and AC cracks, are modeled and analyzed. Because of the asymmetry of the lattice structure of WS_2, the ZZ crack is composed of pairs of S atoms at its outermost atomic layer, whereas the other surface is composed of W atoms (see Figure 2c). The surfaces of AC cracks are symmetric and have two different tip structures: a pair of S atoms (AC-S) or one W atom (AC-W) at their tips (see Figure 2d,e). The build-up models contain 3360−3456 atoms.

2.3. Finite Element Methods. The mechanical performance of the WS_2-based flexible device was analyzed by the finite element model (ANSYS workbench 14.0). The model geometry is shown in Figure 3, which consists of a flexible substrate and electrodes. Because the thickness of the WS_2 thin film is much thinner than that of the substrate and electrodes, and WS_2 is fully covered by the electrodes, the deformation of WS_2 synchronizes with that of the substrate. In this model, we did not consider WS_2 to reduce the number of mesh facets and speed up calculations. The material properties in the WS_2-based flexible device are listed in Table 1. The temperature is set at 25 °C. The boundary condition is assumed that the surface of the substrate has no defects or scratches. The left end is fixed, and the right end is applied with a tensile force F in the x-direction (Figure 4).

Table 1. Material Properties of the Materials in WS_2-Based Flexible Device[a]

item	Au	PET	PI	PDMS
dimension (mm)	N/A	$l \times w \times t$: 50 × 10 × 0.1/0.075/0.05/0.02		
density (kg/m^3)	19,300	2210	1420	1220
Young's module (GPa)	78.5	4.5	2.5	0.0018
Poisson's ratio	0.42	0.37	0.34	0.48

[a] l: length, w: width, t: thickness.

3. RESULTS AND DISCUSSION

3.1. Effects of Defects on the Mechanical Performance of WS_2. At first, the uniaxial tensile analysis was performed on a stand-alone and defect-contained WS_2 at 300 K using the strain rate of 0.001 ps^{-1}. The defects were divided as point defects (2S vacancies and 5−8−5 defect) and line defects (ZZ, AC-S, and AC-W defects). The corresponding stress−strain curves are plotted in Figure 4. By fitting the initial stress−strain curves based on linear regression up to 1% strain, we obtained the corresponding Young's modulus E_x = 113.61 GPa and E_y = 112.35 GPa. Also, the Poisson's ratios were calculated as υ_x = 0.29 and υ_y = 0.30 by the linear fitting of the transverse strain to axial strain curve up to 2% strain. Our work results are in good agreement with those in the literature, that is, 126.1 GPa and υ = 0.27.[29] In addition, the near-degeneracy of the elastic moduli along two orthogonal directions implies that the single-layer WS_2 is a virtually elastic isotropic 2D material because of the threefold rotational symmetry in this quasi-hexagonal lattice structure.[34]

As the applied strain increases, the relationship between stress and strain gradually becomes nonlinear. The maximum stress and its corresponding strain along the AC direction are higher than that along the ZZ direction. The obtained mechanical properties of stand-alone WS_2 defect-free and with S vacancy, 5−8−5, ZZ, AC-S, and AC-W defects are listed in Table 2. The corresponding results are also plotted in Figure 5. The monolayer WS_2 with ZZ cracks is more likely to be broken under the tensile stress along the AC direction, which is of 0.081 critical strain and 4.88 GPa ultimate stress. In the case of the stress along the ZZ direction, WS_2 with AC-S and AC-W line defects tend to be more fragile, which are of 0.080 and 0.082 critical strain, respectively. In contrast, the critical strain of WS_2 with ZZ line defects significantly increased to 0.199. This is because the AC direction expansion of the original line defect releases the localized stress, resulting in several spikes in the stress−strain curve and a higher critical strain. The simulation results show that the crack will seriously degrade

https://dx.doi.org/10.1021/acs.jpcc.0c09897
J. Phys. Chem. C 2021, 125, 2680−2690

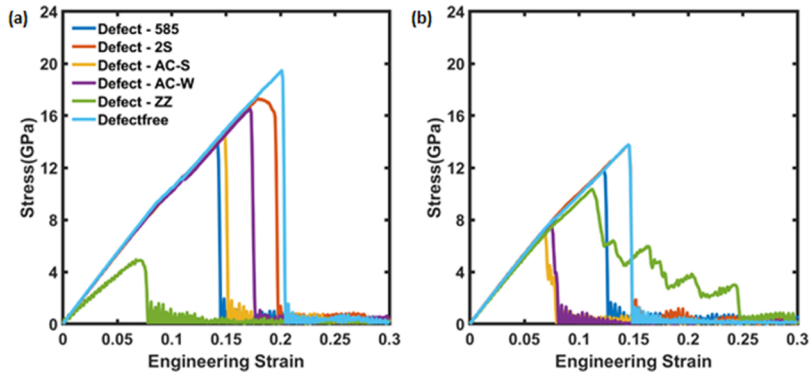

Figure 4. Stress−strain curves of defect-free WS_2, and WS_2 with 2S vacancies, 5−8−5, ZZ, AC-S, and AC-W defects for the tensile loading along (a) AC direction and (b) ZZ direction.

Table 2. Mechanical Properties of Defect-Free WS_2 and WS_2 with S Vacancy, 5−8−5, AC-S, AC-W, and ZZ Defects

		defect-free	2S defect	5−8−5 defect	AC-S defect	AC-W defect	ZZ defect
AC	E (GPa)	107.08	112.53	108.91	95.42	102.81	61.19
	σ (GPa)	19.16	19.94	15.12	15.23	13.53	4.97
	E	0.199	0.220	0.145	0.162	0.152	0.072
ZZ	E (GPa)	105.92	111.93	106.98	106.49	110.90	101.28
	σ (GPa)	14.44	13.50	11.63	8.22	7.16	9.88
	E	0.142	0.149	0.111	0.076	0.075	0.132

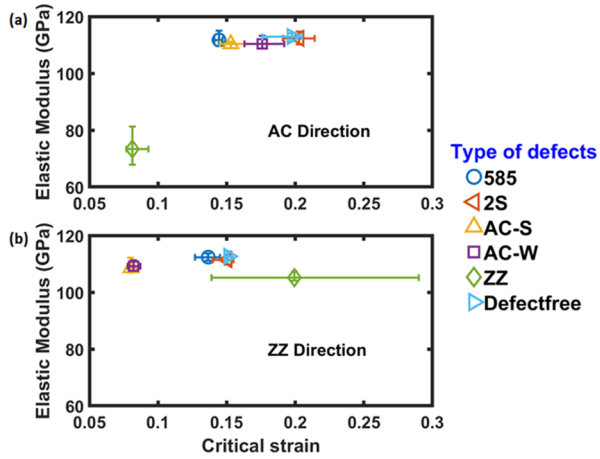

Figure 5. Critical strain and elastic modulus of defect-free WS_2, and WS_2 with 2S vacancies, 5−8−5, AC-S, AC-W, and ZZ defects for the tensile loading along (a) AC direction and (b) ZZ direction.

the mechanical performance of the monolayer WS_2 with stress perpendicular to its extension direction.

In AC-type defects, it can be seen that the ultimate stress of the AC-S crack is greater than that of the AC-W defect, which is mainly because of different interatomic interactions between W−W and S−S atoms in WS_2. As listed in Table S1, the cutoff distance of W−W pairwise interactions ($r_{max\text{-}W\text{-}W}$ = 4.3 Å) is larger than that of S−S interactions ($r_{max\text{-}S\text{-}S}$ = 3.8 Å). Because the distance between the four S atoms at the tip of AC-W is larger than $r_{max\text{-}S\text{-}S}$, they do not interact with each other. On the contrary, the distance between the two W atoms (3.166 Å) at the tip of the AC-S crack is less than $r_{max\text{-}W\text{-}W}$; thus, they interact with each other. As a result, a higher energy is needed to deduce this extra interatomic interaction and deform the crack tip neighborhood, which consequently leads to an increase in the fracture strength. With regard to the 5−8−5 crack, the crack prefers to propagate along the ZZ edge, which has a lower edge energy than the AC edge.[35]

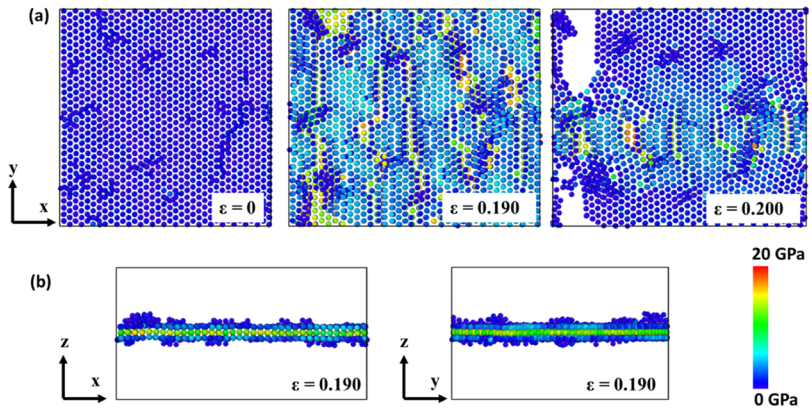

Figure 6. Stress distribution on atoms (a) at the strain of ε = 0.0, 0.190, 0.200 in the AC direction and (b) side view at ε = 0.190 for defect-free WS_2.

https://dx.doi.org/10.1021/acs.jpcc.0c09897
J. Phys. Chem. C 2021, 125, 2680−2690

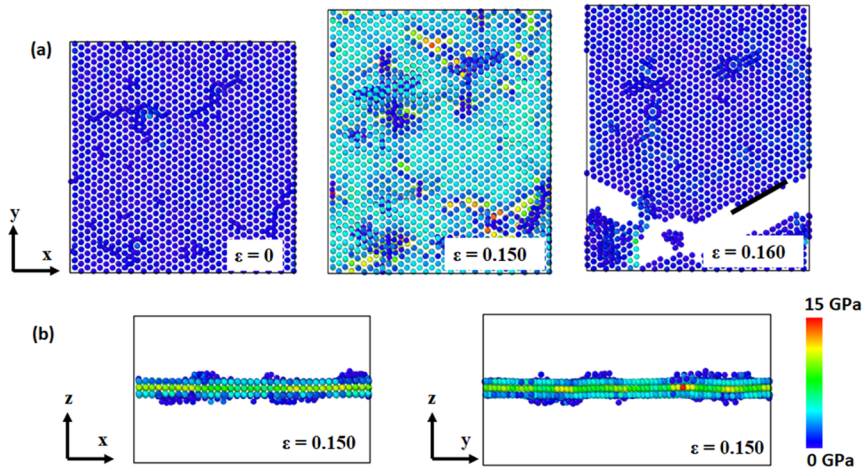

Figure 7. Stress distribution on atoms (a) at the strain of ε = 0.0, 0.150, 0.160 in the ZZ direction and (b) side view at ε = 0.150 for defect-free WS_2.

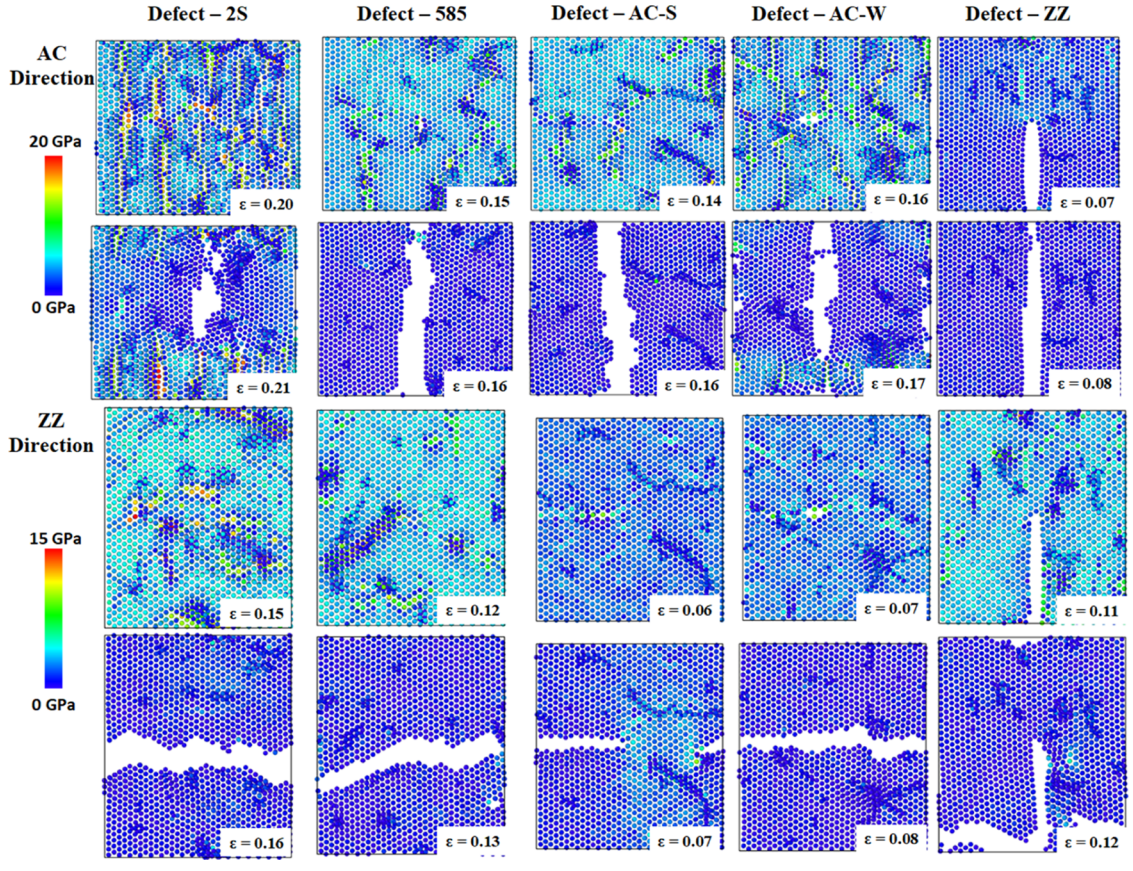

Figure 8. Atomic stress distribution of WS_2 2S vacancies, 5−8−5, AC-S, AC-W, and ZZ defects before and after rupture.

To further study the stress distribution on each atom, the atomic stress map in MD simulations is plotted in Figures 6 and 7 for different loading conditions. The transition from blue to red shows an increase in the magnitude of the atomic stress during tensile deformation. Before the final fracture, the profiles of atomic stress distribution are extracted to reveal the failure mechanism contributed by W and S atoms, respectively. As shown in Figure 6a, several microcracks in the S layers before the fracture appear, and the exposed W atoms exhibit a higher atomic stress than S atoms. From the side view in Figure 6b, it can be verified that S atoms are colored in blue, indicating a low atomic stress, whereas the major stress is concentrated in the W layer. In the loading along the ZZ direction shown in Figure 8, fewer cracks are observed in the S layers and from its profile. It can be found that W atoms also exhibit a higher atomic stress. It is noticeable that the fracture is perpendicular to an AC loading direction but shows 30° in the case of a ZZ loading.

To figure out the influence of defects on the failure mechanism, the atomic stress distribution of each model before and after failure is shown in Figure 8 for the AC and ZZ directions. It can be seen that the final fracture takes place

https://dx.doi.org/10.1021/acs.jpcc.0c09897
J. Phys. Chem. C 2021, 125, 2680−2690

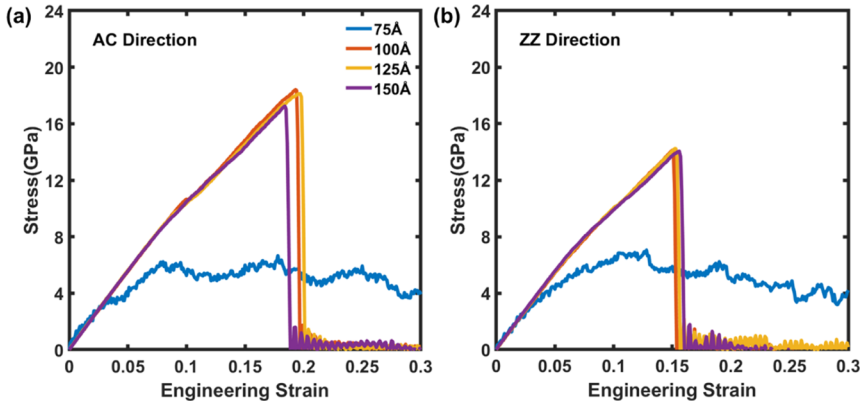

Figure 9. Stress−strain curve of uniaxial tension simulation in defect-free monolayer WS_2 at various dimensions: (a) loading along AC direction; (b) loading along ZZ direction.

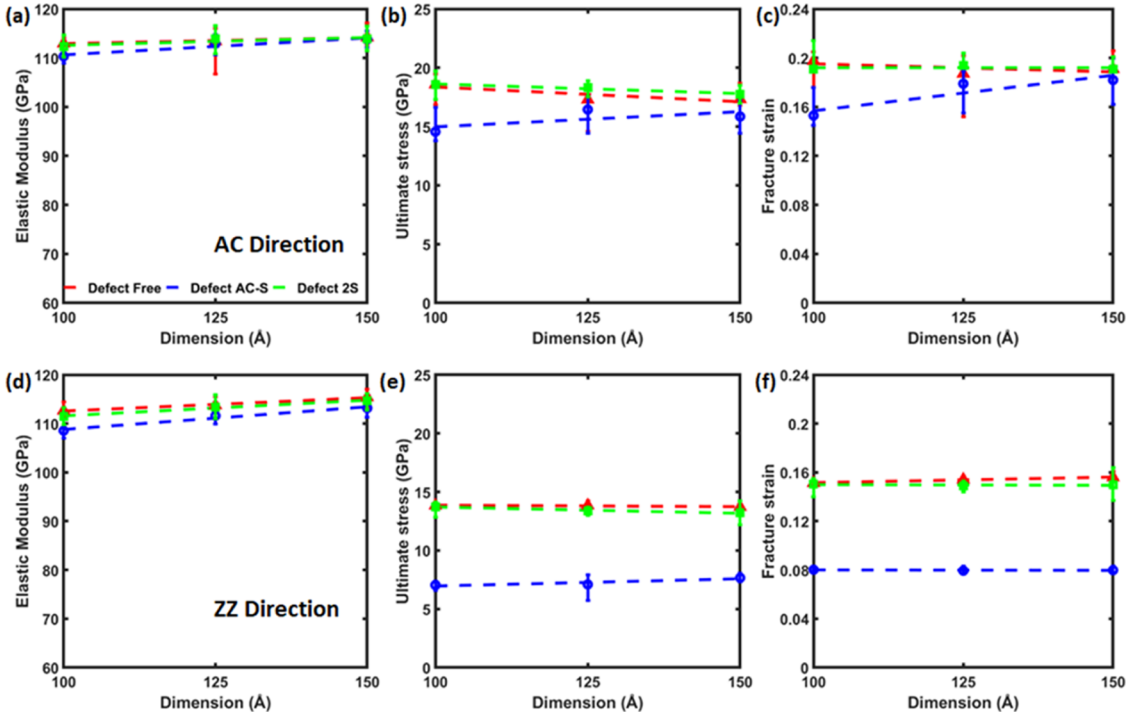

Figure 10. Mechanical properties of the monolayer WS_2 with various defect densities. AC loading direction: (a) elastic modulus; (b) ultimate stress; (c) fracture strain; ZZ loading direction: (d) elastic modulus; (e) ultimate stress; (f) fracture strain.

around the original defects. For the loading along the AC direction, similar to the defect-free model, a large number of cracks appear in S layers, and the stress concentrates in the W layer. The model with 2S defect shows the most cracks, resulting in the largest critical strain. In contrast, fewer cracks in S layers are found in the rest model, indicating a smaller critical strain. Especially in the model of ZZ defect, because of the large initial crack, the extension quickly happens, and WS_2 breaks before many cracks formed in the S layers.

Furthermore, when the loading is in the ZZ direction, in the model of AC-S defect and AC-W defect, the initial defect becomes perpendicular to the loading force, resulting in a small critical strain, as 0.081 and 0.08, respectively. In contrast, the initial defect in the model of ZZ defect is parallel to the loading force. Therefore, the critical strain increases to 0.139, which is approximately twice the number with the AC direction loading, 0.078. It is also noticeable that the final failure takes place on the initial crack in the case of the two AC defect models. In the model of ZZ defect, the failure position is at one end of the manually created ZZ defect. Besides, the models containing point defects present insensitivity to the loading direction. Similar to the defect-free model, the fracture exhibits 30°, and its critical strain is smaller than that of the model with the loading in the AC direction.

The atomic stress distribution near failure in defect-contained models show that point defects have less influence on the failure mechanism but lose the mechanical properties. As for models containing line defects, failure usually takes place on the initial cracks. Its ultimate stress and critical strain significantly degrade when the loading direction is perpendicular to the crack direction.

3.2. Effect of Defect Density on the Mechanical Performance of WS_2. To comparatively analyze the effects of defect densities, a single defect was put in various simulation systems with different dimensions to change the defect densities. The convergence of the mechanical properties with

https://dx.doi.org/10.1021/acs.jpcc.0c09897
J. Phys. Chem. C 2021, 125, 2680−2690

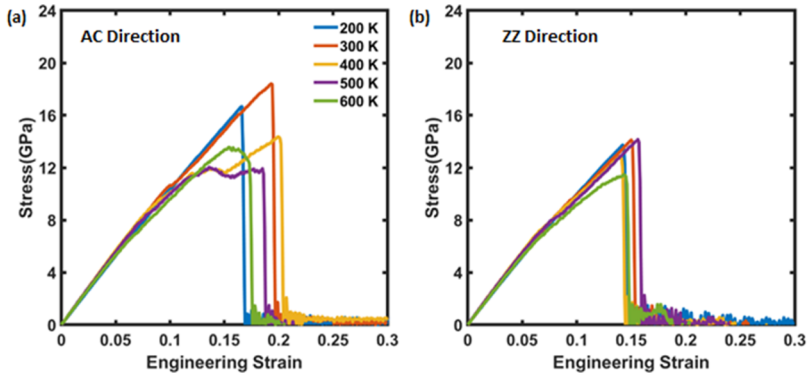

Figure 11. Stress−strain curve of uniaxial tension simulation in the defect-free monolayer WS_2 at various temperatures: (a) loading along the AC direction; (b) loading along the ZZ direction.

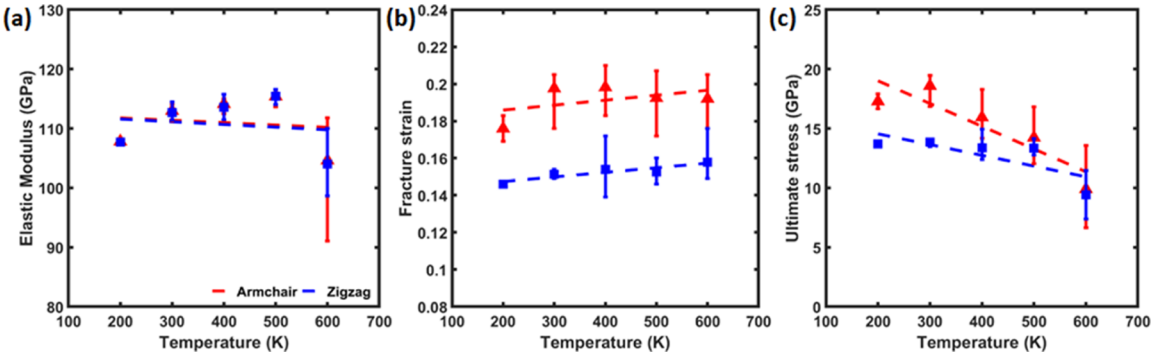

Figure 12. Mechanical properties of the monolayer WS_2 at different temperatures. (a) Young's modulus vs temperature; (b) fracture strain vs temperature; (c) ultimate stress vs temperature.

system dimensions was first verified with the defect-free model, as shown in Figure 9. It is found that the simulation system fell to equilibrium with a dimension of 75 Å, whereas the dimension over 100 Å presents a consistent result. As a result, a simulation system with 100 Å dimension contains sufficient atoms and therefore is proper to simulate tension under various conditions.

Then, the tension simulations of the three models along the AC and ZZ directions were conducted in different-sized simulation boxes. The mechanical properties are plotted in Figure 10, where each point presents five data, and the dashed line is the fitting line to the average values. It can be seen that the model with no defect and the one with 2S defect show similar mechanical properties and slight changes according to different-sized simulation systems. This is because the missing S atom takes a negligible percentage to the whole system, such as 0.06, 0.04, and 0.03% in the simulation system, with dimensions of 100, 125, and 150 Å, respectively.

However, in the case of the AC-S defect model, the defect density is higher than the 2S defect model because of the line defect. The missing atoms in the line defect occupy 0.72, 0.62, and 0.54% in the three sized simulation systems. Therefore, in a larger simulation system, the defect density correspondingly decreases, resulting in a closer elastic modulus to the defect-free model as well as the 2S defect model. As for the ultimate stress and fracture strain, similar phenomena are observed along the AC direction such that the numbers in a 150 Å sized simulation system have neglect differences. In contrast, the obtained ultimate stress and fracture strain with ZZ direction loading present noticeable gaps compared to the obtained values in either the defect-free model or 2S defect model, although a slight increase is still observed. It is due to the different fracture mechanism that has been described in Section 3.1.

Therefore, it can be concluded that a lower defect density indicates improved elastic modulus, close to a defect-free model. As for the ultimate stress and fracture strain, which are not the material's intrinsic properties, defect density plays a less important role in the case of a line defect model because of the failure mechanism.

3.3. Effect of Temperature on the Mechanical Performance of WS_2. To study the effect of temperature on the mechanical behavior of the defect-free WS_2, MD simulations of tensile tests are performed in the temperature range of 200−600 K with an increment of 100 K. The corresponding stress−strain curves are plotted in Figure 11 for AC and ZZ loading directions. It can be seen that under loading along the AC direction, the ultimate stress decreases with an increase in temperature. However, under a ZZ direction loading, the ultimate stress changes slightly in the temperature range of 200−400 K. To obtain a better understanding of the effects of temperature, the values of the fracture strength, fracture strain, and Young's modulus of the monolayer WS_2 as a function of temperature are plotted in Figure 12, where each point represents the average of five points. As shown in Figure 11a, the loading direction has less influence on the elastic modulus, whereas the promotion caused by temperature is observed before 500 K. At 600 K, degradation from 115.39 to 104.62 and from 115.42 to 104.03 GPa is found in the AC and ZZ loading directions, respectively. As shown in Figure 12a, the loading direction has less influence on the elastic modulus, whereas the

https://dx.doi.org/10.1021/acs.jpcc.0c09897
J. Phys. Chem. C 2021, 125, 2680−2690

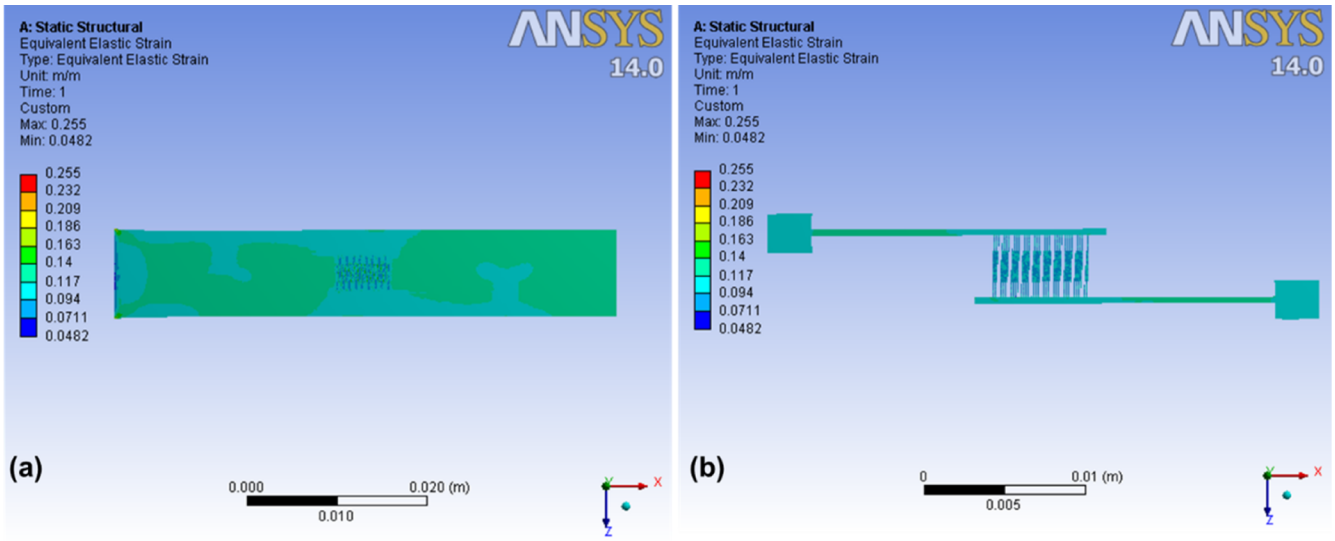

Figure 13. Equivalent elastic strain distribution of (a) the WS_2 PET device and (b) its electrodes under 400 N tensile force in x direction.

promotion caused by temperature is observed before 500 K. At 600 K, degradation from 115.39 to 104.62 and 115.42 to 104.03 GPa is found in the AC and ZZ loading directions, respectively. Besides, it is seen in Figure 12b that as the temperature increases from T = 200 K to T = 600 K, the fracture strain shows a slight increase in both loading directions, and the ductility along the AC loading direction is higher than the number along the ZZ direction at all tension temperatures. As for the ultimate stress, in contrast, in Figure 12c, a significant decrease from 17.28 to 9.89 GPa is found along the AC direction. Similarly, with the temperature increasing to 600 K, this number also experiences a slighter decrease from 13.70 to 9.43 GPa along the AC direction.

The effect of temperature on the strength of the monolayer WS_2 is analyzed as follows. First, according to the Arrhenius equation, the lifetime τ has an exponential function with the tensile stress σ and temperature T[36,37]

$$\tau(\sigma, T) = \tau_0 \exp\left(\frac{U_0 - \gamma\sigma}{kT}\right) \tag{2}$$

where τ_0 is the average period of vibrations of atoms in solids, which is approximately 10^{-13} s, U_0 is the fracture activation energy, and γ is the product of the activation volume and the coefficient of local overstresses, and k is the Boltzmann's constant. The term $U_0 - \gamma\sigma$ means that the energy barrier for brittle fracture can be lowered by increasing the tensile stress. Based on this function, Chung et al.[35] calculated the ultimate tensile stress σ_{uts} of graphene/silicene/graphene heterostructures as below:

$$\sigma_{uts} = \frac{U_0}{\gamma} - \frac{kT}{\gamma}\ln\left(\frac{kT}{\gamma\tau_0 E\dot{\varepsilon}}\right) \tag{3}$$

where E is Young's modulus and $\dot{\varepsilon}$ is the constant strain rate. Because the variation of the logarithmic term with temperature is negligible, σ_{uts} can be approximated as a linear function of temperature. This formula can be used for WS_2, as shown in Figure 12; the linear plot suggests that the kinetic process leading to WS_2 can be broken down into elementary events, where the thermal vibration of the atoms leads to bond dissociation.

Therefore, it can be concluded that different loading directions exhibit different sensitivities to temperature that the ZZ direction is less influenced by temperature compared to the AC direction. Thus, in the experimental design, loading along the ZZ direction is recommended to be applied to WS_2. Besides, the applied strain less than 0.14 and stress less than 10 GPa can be adopted as the boundary conditions in the practical tension experiments.

3.4. Effects of the Substrate on the Mechanical Performance of WS_2-Based Devices. *3.4.1. Theoretical Analysis.* The performance of the strain sensor can be evaluated according to the GF, which is the ratio of relative change in electrical resistance (R) to the mechanical strain ε (GF = $(\Delta R/R_0)/\varepsilon$). Thus, in our case, the GF of the WS_2 strain sensor can be expressed as

$$GF_{sensor} = (\Delta R_{total}/R_{total})/\varepsilon_x$$

where $R_{total} = R_{WS2} + R_{Au}$

$$\Delta R_{total} = \Delta R_{WS2} + \Delta R_{Au}$$

As the Au electrode offers very little resistance, $\Delta R_{Au} \approx 0$, $R_{Au} \approx 0$

$$GF_{sensor} = (\Delta R_{WS2}/R_{WS2})/\varepsilon_x$$

where the tensile strain ε_x is $\varepsilon_x = F/(E\Delta S)$, F is the tensile force, E is Young's modulus of the substrate, and S is the cross-sectional area of the substrate.

It is obvious that GF_{sensor} depends on the electronic properties of WS_2 as well as the mechanical properties (dimensions and Young's modulus) of the substrate. Therefore, we analyzed the mechanical properties of the WS_2 PET strain sensor as an example. The FEA model and methods are described in Section 2.3. The left end is fixed, and the right end is applied with a tensile force F of 400 N in the x direction. As shown in Figure 13, the WS_2 PET device is with a length of 50 mm, width of 10 mm, and thickness of 75 μm. When F increases to 400 N, the maximum equivalent elastic strain in the center of the device can reach the critical strain of WS_2, 0.1. The equivalent elastic strain of WS_2 flexible devices is shown in Figure 13, which reveals that the strain in the center of the sensor is affected by the strain of the electrodes.

https://dx.doi.org/10.1021/acs.jpcc.0c09897
J. Phys. Chem. C 2021, 125, 2680−2690

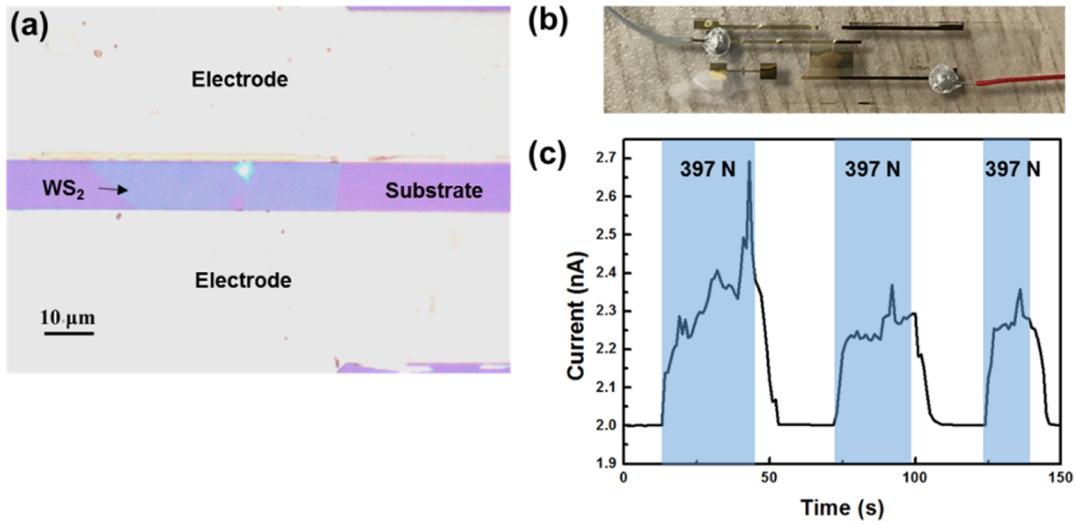

Figure 14. Optical images of (a) WS_2 thin film under Au electrodes and (b) WS_2 strain sensor with the PET substrate. (c) Dynamic current change under tensile strain. In the blue area, 397 N tensile force was applied to the sample.

3.4.2. Benchmark Analysis. For benchmarking the FEA results, we fabricated a WS_2 strain sensor in a PET substrate. As shown in Figure 14, a chemical vapor deposition-grown WS_2 thin film was transferred to the center of the PET substrate. Then, Au electrodes were deposited to the top of the WS_2 thin film through the thermal evaporation process, followed by a lift-off process. The thickness of the WS_2 thin film is about 10 nm, as shown in Figure S1. The flowchart of the fabrication process is shown in Figure S2. The tensile test was carried out through a homemade fixture (see Figure S3). The real-time current change was reported by a source meter (Keithley 2400). The measurement results show that the current of the WS_2 sensor increases when applying tensile strain, which is consistent with the increased conductivity of WS_2 calculated from the first-principles analysis. The response time is shorter than 10 s. It indicates that WS_2 has potential applications in the strain sensor. However, the current change is so small, only 0.5 nA, which is associated with the slight deformation of the substrate under 397 N tensile force. The strain of PET is around 0.07, which is consistent with the strain value in the center of the FEA model. It means that our multiscale analysis can be used for benchmarking the flexible device.

3.4.3. Optimization of the Substrate. Because the deformation of the substrate for the WS_2 sensor is too small, it is necessary to optimize the WS_2 structure to obtain a higher GF. FEA was carried out to comparatively analyze the relationship between the mechanical properties of the substrate and tensile force (F). It is clear that the thicker the substrate, the higher F is required to reach the critical strain of 0.1. We should reduce the cross-sectional area of the substrate ($S = w \times t$, w: width, t: thickness) to decrease F. It can also be found that F depends on Young's module E of the substrate when S and ε_x are fixed. In this case, it is better to choose one substrate with low E to achieve a higher GF (Figure 15).

3.4.4. Effects of Defects on the Electrical Performance of WS_2. As the band structure can reveal the conductivity of a material, the strains in AC (x) and ZZ (y) directions are carried out for the monolayer WS_2 by fixing one lattice constant and changing the other. As shown in Figure 16, the electronic structures vary significantly by the strain in both defect-free and point defect-contained WS_2. The band gap

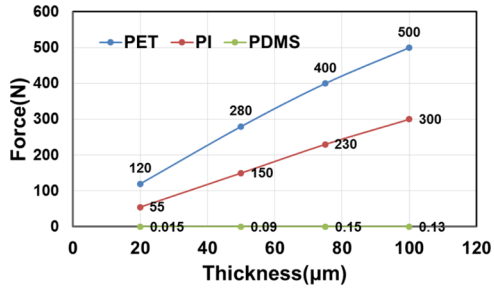

Figure 15. Thickness–tensile force curve for different types of substrates.

energy (E_g) decreases linearly when the strain increases from 0 to 1% in AC and ZZ directions. In the case of the defect-free model, the band gap decreases from 1.906 to 1.167 eV in the AC direction and to 1.137 eV in the ZZ direction, whereas after introducing two S vacancies, this number drops from 0.716 to 0.403 and 0.514 eV along the AC and ZZ directions, respectively. According to the classical relation between E_g and the electrical conductivity (σ) of materials,[38]

$$\sigma \propto e^{(-E_g/2kT)} \quad (4)$$

where k and T are Boltzmann's constant and the temperature, respectively. Clearly, a lower E_g indicates a higher σ at the given temperature. Thus, the conductivity of the WS_2-based device increases after applying tensile strain. This is consistent with the experimental results. Moreover, defects can result in a narrower band gap of WS_2, which induces a higher current.

4. CONCLUSIONS

This work systematically analyzes the mechanical properties of WS_2 on a multiscale. The mechanical properties (i.e., Young's modulus and critical stress) of WS_2 under different strains are analyzed by MD. The influence of different defect types (i.e., point defects and line defects), defect density, and different ambient temperatures on the mechanical properties are discussed. To figure out the influence of defects on the failure mechanism, the atomic stress distribution of each model before and after a fracture is studied. The results reveal that the performance of line defect models is sensitive to the loading

https://dx.doi.org/10.1021/acs.jpcc.0c09897
J. Phys. Chem. C 2021, 125, 2680–2690

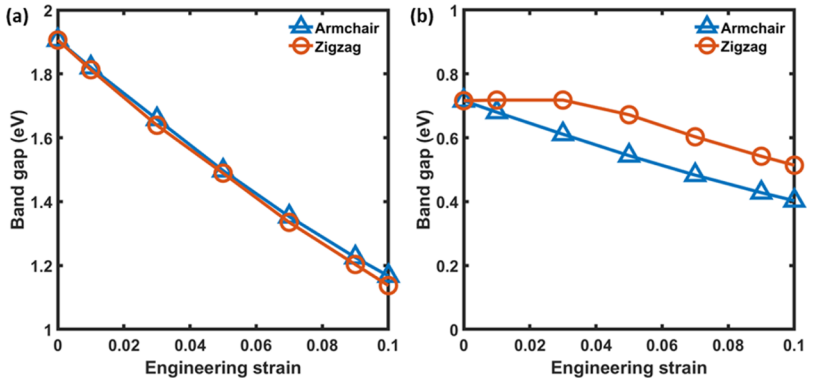

Figure 16. Band gap of (a) defect-free WS_2 and (b) WS_2 with 2S vacancies under strain in AC and ZZ directions.

direction, regardless of the defect density. Temperature also plays an essential role in deciding its performance, as high temperature results in better ductility but strength. Also, a peak of elastic modulus is found at 500 K. Then, we discuss the effects of different substrates on the flexible WS_2 device through FEA. Finally, a WS_2 strain sensor based on PET was fabricated for benchmarking the first-principles analysis and FEA results. The deformation of PET agrees with the FEA results. As the strain increased, the current of the sensor gradually increased, which was verified with the DFT results. The band gap changes of WS_2 under different strains are analyzed through the first-principles analysis. The results show that as the strain increases, the band gap becomes smaller. The conductivity consequently increases. This proves that this multiscale simulation method can efficiently analyze the mechanical properties of 2D materials with and without defects. This method can provide a prediction of mechanical performances of WS_2 at atomic, molecular, and device levels, which can be extended to analyze all other 2D materials.

■ ASSOCIATED CONTENT

Supporting Information

The Supporting Information is available free of charge at https://pubs.acs.org/doi/10.1021/acs.jpcc.0c09897.

Two-body (bond-bending) SW potential parameters for GULP; three-body (angle-bending) SW potential parameters for GULP; SW potential parameters for LAMMPs; and LAMMPS input files for tension simulations (PDF)

■ AUTHOR INFORMATION

Corresponding Author

Guoqi Zhang − *Department of Microelectronics, Faculty of Electrical Engineering, Mathematics & Computer Science, Delft University of Technology, Delft 2628 CT, the Netherlands*; Email: G.Q.Zhang@tudelft.nl

Authors

Hongyu Tang − *Department of Microelectronics, Faculty of Electrical Engineering, Mathematics & Computer Science, Delft University of Technology, Delft 2628 CT, the Netherlands*; orcid.org/0000-0002-2720-6709

Dong Hu − *Department of Microelectronics, Faculty of Electrical Engineering, Mathematics & Computer Science, Delft University of Technology, Delft 2628 CT, the Netherlands*; orcid.org/0000-0002-3739-5750

Zhen Cui − *Department of Microelectronics, Faculty of Electrical Engineering, Mathematics & Computer Science, Delft University of Technology, Delft 2628 CT, the Netherlands*

Huaiyu Ye − *School of Microelectronics, Southern University of Science and Technology, Shenzhen 518055, China; Shenzhen Institute of Wide-bandgap Semiconductors, Shenzhen 518055, Guangdong, China*; orcid.org/0000-0002-0385-4728

Complete contact information is available at: https://pubs.acs.org/10.1021/acs.jpcc.0c09897

Author Contributions

‖H.T. and D.H. contributed equally to this work.

Notes

The authors declare no competing financial interest.

■ ACKNOWLEDGMENTS

This work was supported by the National Key R&D Program of China (2018YFE0204600), the Key-Area Research and Development Program of GuangDong Province (2019B010131001), and the Shenzhen Key Project for Basic Research (JCYJ20200109140822796).

■ REFERENCES

(1) Novoselov, K. S.; Geim, A. K.; Morozov, S. V.; Jiang, D.; Zhang, Y.; Dubonos, S. V.; Grigorieva, I. V.; Firsov, A. A. Electric Field Effect in Atomically Thin Carbon Films. *Science* **2004**, *306*, 666.

(2) Iguiñiz, N.; Frisenda, R.; Bratschitsch, R.; Castellanos-Gomez, A. Revisiting the Buckling Metrology Method to Determine the Young's Modulus of 2D Materials. *Adv. Mater.* **2019**, *31*, 1807150.

(3) Mehew, J. D.; Unal, S.; Torres Alonso, E.; Jones, G. F.; Fadhil Ramadhan, S.; Craciun, M. F.; Russo, S. Fast and Highly Sensitive Ionic-Polymer-Gated WS2 -Graphene Photodetectors. *Adv. Mater.* **2017**, *29*, 1700222.

(4) Wang, G.; Li, L.; Fan, W.; Wang, R.; Zhou, S.; Lü, J.-T.; Gan, L.; Zhai, T. Interlayer Coupling Induced Infrared Response in WS2 /MoS2 Heterostructures Enhanced by Surface Plasmon Resonance. *Adv. Funct. Mater.* **2018**, *28*, 1800339.

(5) Kang, K.; Godin, K.; Kim, Y. D.; Fu, S.; Cha, W.; Hone, J.; Yang, E.-H. Graphene-Assisted Antioxidation of Tungsten Disulfide Monolayers: Substrate and Electric-Field Effect. *Adv. Mater.* **2017**, *29*, 1603898.

(6) Tang, H.; et al. Ultra-High Sensitive No2 Gas Sensor Based on Tunable Polarity Transport in Cvd-Ws2/Igzo P-N Heterojunction. *ACS Appl. Mater. Interfaces* **2019**, *11*, 40850−40859.

(7) Tang, H.; Tan, C.; Yang, H.; Zheng, K.; Li, Y.; Ye, H.; Chen, X.; Fan, X.; Ren, T.; Zhang, G. Tunable Electronic and Optical Properties of the Ws2/Igzo Heterostructure Via an External Electric Field and

Strain: A Theoretical Study. *Phys. Chem. Chem. Phys.* **2019**, *21*, 14713−14721.
(8) Wang, X.; Dong, L.; Zhang, H.; Yu, R.; Pan, C.; Wang, Z. L. Recent Progress in Electronic Skin. *Adv. Sci.* **2015**, *2*, 1500169.
(9) Liu, K.; et al. Elastic Properties of Chemical-Vapor-Deposited Monolayer Mos2, Ws2, and Their Bilayer Heterostructures. *Nano Lett.* **2014**, *14*, 5097−5103.
(10) Zhang, Q.; Chang, Z.; Xu, G.; Wang, Z.; Zhang, Y.; Xu, Z.-Q.; Chen, S.; Bao, Q.; Liu, J. Z.; Mai, Y.-W.; Duan, W.; Fuhrer, M. S.; Zheng, C. Strain Relaxation of Monolayer WS2 on Plastic Substrate. *Adv. Funct. Mater.* **2016**, *26*, 8707−8714.
(11) Guo, H.; Lan, C.; Zhou, Z.; Sun, P.; Wei, D.; Li, C. Transparent, Flexible, and Stretchable Ws2 Based Humidity Sensors for Electronic Skin. *Nanoscale* **2017**, *9*, 6246−6253.
(12) Qi, H.-Y.; Mi, W.-T.; Zhao, H.-M.; Xue, T.; Yang, Y.; Ren, T.-L. A Large-Scale Spray Casting Deposition Method of Ws2 Films for High-Sensitive, Flexible and Transparent Sensor. *Mater. Lett.* **2017**, *201*, 161−164.
(13) Jeong, H. Y.; Jin, Y.; Yun, S. J.; Zhao, J.; Baik, J.; Keum, D. H.; Lee, H. S.; Lee, Y. H. Heterogeneous Defect Domains in Single-Crystalline Hexagonal Ws2. *Adv. Mater.* **2017**, *29*, 1605043.
(14) Zhao, X.; Dai, X.; Xia, C.; Wang, T. Structural Defects in Pristine and Mn-Doped Monolayer Ws2: A First-Principles Study. *Superlattices Microstruct.* **2015**, *85*, 339−347.
(15) Schuler, B.; et al. How Substitutional Point Defects in Two-Dimensional WS2 Induce Charge Localization, Spin-Orbit Splitting, and Strain. *ACS Nano* **2019**, *13*, 10520−10534.
(16) Wang, X.; Tabarraei, A.; Spearot, D. E. Fracture Mechanics of Monolayer Molybdenum Disulfide. *Nanotechnology* **2015**, *26*, 175703.
(17) Talebi, H.; Silani, M.; Bordas, S. P. A.; Kerfriden, P.; Rabczuk, T. A Computational Library for Multiscale Modeling of Material Failure. *Comput. Mech.* **2014**, *53*, 1047−1071.
(18) Budarapu, P. R.; Gracie, R.; Yang, S.-W.; Zhuang, X.; Rabczuk, T. Efficient Coarse Graining in Multiscale Modeling of Fracture. *Theor. Appl. Fract. Mech.* **2014**, *69*, 126−143.
(19) Dadrasi, A.; Albooyeh, A. R.; Mashhadzadeh, A. H. Mechanical Properties of Silicon-Germanium Nanotubes: A Molecular Dynamics Study. *Appl. Surf. Sci.* **2019**, *498*, 143867.
(20) Ahangari, M. G.; Mashhadzadeh, A. H.; Fathalian, M.; Dadrasi, A.; Rostamiyan, Y.; Mallahi, A. Effect of Various Defects on Mechanical and Electronic Properties of Zinc-Oxide Graphene-Like Structure: A Dft Study. *Vacuum* **2019**, *165*, 26−34.
(21) Ghorbanzadeh Ahangari, M.; Salmankhani, A.; Imani, A. H.; Shahab, N.; Hamed Mashhadzadeh, A. Density Functional Theory Study on the Mechanical Properties and Interlayer Interactions of Multi-Layer Graphene: Carbonic, Silicon-Carbide and Silicene Graphene-Like Structures. *Silicon* **2019**, *11*, 1235−1246.
(22) Hamed Mashhadzadeh, A.; Fereidoon, A.; Ghorbanzadeh Ahangari, M. Combining Density Functional Theory-Finite Element Multi-Scale Method to Predict Mechanical Properties of Polypropylene/Graphene Nanocomposites: Experimental Study. *Mater. Chem. Phys.* **2017**, *201*, 214−223.
(23) Kumar, H.; Er, D.; Dong, L.; Li, J.; Shenoy, V. B. Elastic Deformations in 2d Van Der Waals Heterostructures and Their Impact on Optoelectronic Properties: Predictions from a Multiscale Computational Approach. *Sci. Rep.* **2015**, *5*, 10872.
(24) Luan, Q.; Yang, C.-L.; Wang, M.-S.; Ma, X.-G. First-Principles Study on the Electronic and Optical Properties of Ws2 and Mos2 Monolayers. *Chin. J. Phys.* **2017**, *55*, 1930−1937.
(25) Bui, V. Q.; Pham, T.-T.; Le, D. A.; Thi, C. M.; Le, H. M. A First-Principles Investigation of Various Gas (Co, H2o, No, and O2) Absorptions on a Ws2monolayer: Stability and Electronic Properties. *J. Phys.: Condens. Matter* **2015**, *27*, 305005.
(26) Delley, B. From Molecules to Solids with the Dmol3 Approach. *J. Chem. Phys.* **2000**, *113*, 7756−7764.
(27) Debbichi, L.; Eriksson, O.; Lebègue, S. Electronic Structure of Two-Dimensional Transition Metal Dichalcogenide Bilayers from Ab Initio Theory. *Phys. Rev. B: Condens. Matter Mater. Phys.* **2014**, *89*, 205311.
(28) Plimpton, S. Fast Parallel Algorithms for Short-Range Molecular Dynamics. *J. Comput. Phys.* **1995**, *117*, 1−19.
(29) Mobaraki, A.; Kandemir, A.; Yapicioglu, H.; Gülseren, O.; Sevik, C. Validation of Inter-Atomic Potential for Ws2 and Wse2 Crystals through Assessment of Thermal Transport Properties. *Comput. Mater. Sci.* **2018**, *144*, 92−98.
(30) Ma, L.; Tan, Y.; Ghorbani-Asl, M.; Boettger, R.; Kretschmer, S.; Zhou, S.; Huang, Z.; Krasheninnikov, A. V.; Chen, F. Tailoring the Optical Properties of Atomically-Thin Ws2via Ion Irradiation. *Nanoscale* **2017**, *9*, 11027−11034.
(31) Zhang, Z.; Xie, Y.; Peng, Q.; Chen, Y. A Theoretical Prediction of Super High-Performance Thermoelectric Materials Based on Mos2/Ws2 Hybrid Nanoribbons. *Sci. Rep.* **2016**, *6*, 21639.
(32) Surblys, D.; Matsubara, H.; Kikugawa, G.; Ohara, T. Application of Atomic Stress to Compute Heat Flux Via Molecular Dynamics for Systems with Many-Body Interactions. *Phys. Rev. E* **2019**, *99*, 051301.
(33) Stukowski, A. Visualization and analysis of atomistic simulation data with OVITO-the Open Visualization Tool. *Modell. Simul. Mater. Sci. Eng.* **2009**, *18*, 015012.
(34) Born, M.; Huang, K.; Lax, M. Dynamical Theory of Crystal Lattices. *Am. J. Phys.* **1955**, *23*, 474.
(35) Chung, J.-Y.; Sorkin, V.; Pei, Q.-X.; Chiu, C.-H.; Zhang, Y.-W. Mechanical Properties and Failure Behaviour of Graphene/Silicene/Graphene Heterostructures. *J. Phys. D: Appl. Phys.* **2017**, *50*, 345302.
(36) Wei, C.; Cho, K.; Srivastava, D. Tensile Strength of Carbon Nanotubes under Realistic Temperature and Strain Rate. *Phys. Rev. B: Condens. Matter Mater. Phys.* **2003**, *67*, 115407.
(37) Slutsker, A. I.; Betekhtin, V. I.; Lee, J. C.; Yusupov, D.; Kadomtsev, A. G.; Amosova, O. V. Temperature Dependence of Rupture Strength of the Amorphous Alloy Ni82.1cr7.8si4.6fe3.1m-n0.3al0.1cu<0.1b2. *Acta Mater.* **2004**, *52*, 2733−2738.
(38) Roondhe, B.; Jha, P. K. "Haeckelite", a New Low Dimensional Cousin of Boron Nitride for Biosensing with Ultra-Fast Recovery Time: A First Principles Investigation. *J. Mater. Chem. B* **2018**, *6*, 6796−6807.

https://dx.doi.org/10.1021/acs.jpcc.0c09897
J. Phys. Chem. C 2021, 125, 2680−2690